DOI: https://doi.org/10.68732/b13f52006a66ad6d

ISBN: 978-9989-2053-7-8

Research on Deformation Characteristics and Instability Mechanism of Retrogressive Landslide Under the Coupling of Engineering Disturbance and Rainfall

Yanhong Zhu[1]& Jiansong Shi[23] & Chuanke Xu[1] & Shengyun Huang[23] & Yang Yu[23]

1. Sinohydro Bureau 7 Co., Ltd. International Engineering Corporation, Chendu, China
2. North China Engineering Investigation Institute Co., Ltd., Shijiazhuang, Hebei, China;
3. Technology Innovation Center for Groundwater Disaster Prevention and Control Engineering for Metal Mines, Ministry of Natural Resources, Shijiazhuang, China.
5121636@qq.com

Abstract

Taking the landslide at section K2+550–K3+420 of a highway in North Macedonia as a case study, this paper systematically analyzes the deformation evolution and failure mechanism of a retrogressive landslide through integrated methods including surface crack investigation, surface and deep displacement monitoring, and MIDAS numerical simulation. The results indicate that typical arc-shaped tension cracks developed at the rear edge of the landslide. Monitoring data reveal that the main sliding direction ranges from 110° to 162°, with a maximum cumulative displacement of 310.2 mm. The deformation process exhibits a three-stage pattern characterized by "steady-rate deformation – accelerated deformation – accelerated creep." Deep displacement monitoring identified the slip surface at a depth of 38 m, located within the completely to strongly weathered phyllite layer. Numerical simulation results demonstrate that excavation unloading induced stress concentration at the slope toe. When superimposed with rainfall infiltration, the strength of the slip zone decreased, causing the factor of safety to drop from 1.16 to 1.04 and leading to the coalescence of the slip surface. The failure mechanism of the landslide can be summarized as: "Excavation unloading dominance → Local yielding → Rainfall infiltration softening → Progressive coalescence → Overall sliding." The findings provide a reference for the mechanism analysis and mitigation design of deep-seated retrogressive landslides.

Keywords

Retrogressive landslide, Deformation monitoring, Numerical simulation, Excavation unloading, Sliding surface.

1 Introduction

The excavation of cutting slopes in mountainous highway construction often disrupts the original mechanical equilibrium of the slope, inducing retrogressive landslides. The deformation of such landslides progresses from the slope toe upward, and the failure mechanism is complex (Yinet al., 2000; Zheng et al., 2007). Combining surface and deep displacement monitoring with numerical simulation (Xu et al., 2003; Xu et al., 2025) has become an effective approach to deeply understanding the instability mechanism of these landslides. This paper takes a typical retrogressive landslide on an expressway in North Macedonia as a case study. Based on field investigation, multi-method monitoring, and MIDAS simulation (Chen et al., 2003; Zheng et al., 2012; Zhang et al., 2019; Wang et al., 2021), this study reveals the progressive coupling instability mechanism of "excavation-rainfall," aiming to provide a reference for similar engineering projects.

2 Overview of the Study Area

The study area is located southwest of Kichevo City, North Macedonia, with an average annual rainfall of 823 mm. The original slope gradient ranges from 17° to 27°. The strata consist of Paleozoic metamorphic rock series, which are, from top to bottom, residual slope soil, completely to strongly weathered phyllite, and quartz-graphite schist. The phyllite has a high content of clay minerals and is easily softened upon contact with water, making it the dominant controlling stratum for the landslide. The landslide plane exhibits a horseshoe shape and is divided into Zones I and II, with a total volume of approximately 61×10^4 m³, classifying it as a deep-seated large-scale landslide. Affected by two phases of cutting excavation, arc-shaped tension cracks have developed at the rear edge of the landslide, with en-echelon cracks arranged along the lateral margins. The landslide is currently in a creeping deformation state (see Fig. 1).

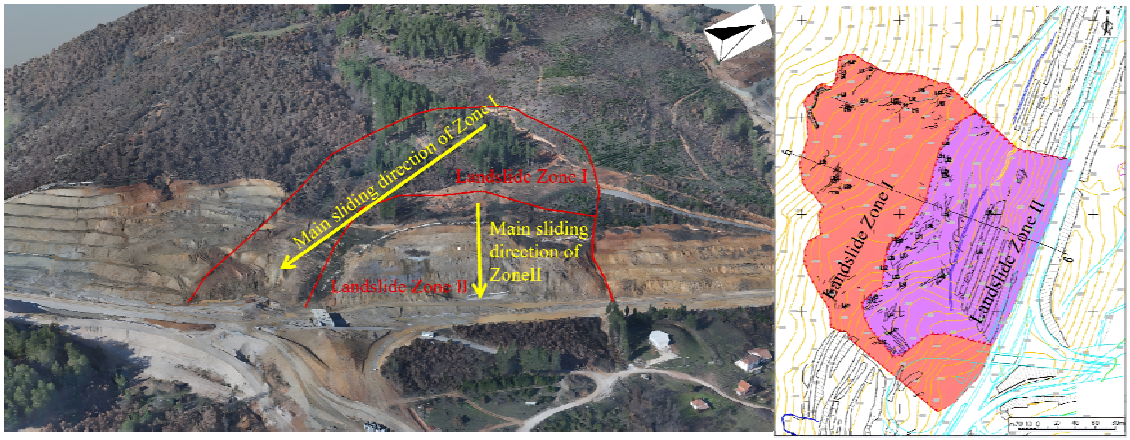


Fig. 1 Full view and zoning map of the landslide.

3 Analysis of Landslide Deformation Characteristics

3.1 Characteristics of Surface Crack Distribution

A total of 50 major cracks were identified during the field investigation, predominantly tensile in nature. Cracks at the rear edge are distributed in an arc shape, with maximum apertures reaching up to 38 cm and vertical offsets of 0.2–3 m. Cracks along the lateral margins exhibit an en-echelon arrangement. Bulging cracks are observed in the central part. This crack assemblage represents a typical response of a retrogressive landslide, characterized by initial sliding at the slope toe followed by tensile cracking at the rear edge due to traction (see Fig. 2).

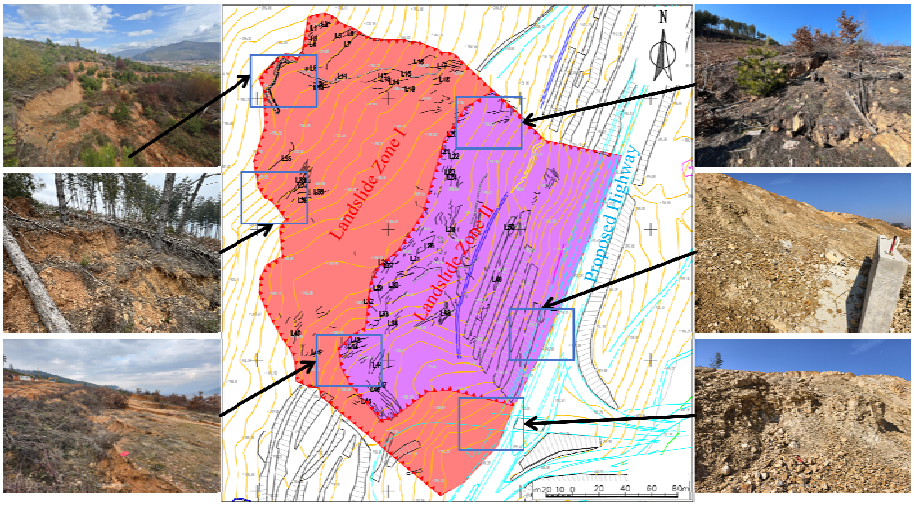


Fig. 2 Distribution map of landslide cracks.

3.2 Surface and Deep Displacement Monitoring

Five monitoring points (M1–M5) were established, with an observation period from February 24 to May 14, 2025. Monitoring point M3 exhibited the maximum cumulative horizontal displacement, reaching 310.2 mm, with a primary sliding direction of 118° and an average rate of 3.83 mm/d. After March 10, the displacement rate increased significantly (>4.5 mm/d), which correlates with the softening of the sliding zone caused by concurrent heavy rainfall. The displacement-time curve (see Fig. 3) exhibits typical three-stage characteristics: constant velocity deformation (Feb 24 – Mar 10, 2.75 mm/d), accelerated deformation (Mar 10 – Apr 22, 4.59 mm/d), and accelerated creep (Apr 22 – May 14, 3.04 mm/d). The displacement distribution is non-uniform, with the maximum values occurring in the thick central portion of the sliding mass, while the sliding direction remains stable.

Deep displacement monitoring at borehole BH11 revealed a distinct displacement mutation at a depth of 38 m (see Fig. 4), indicating that the sliding surface is located within the strongly weathered phyllite layer. The sliding zone soil is muddy in texture, and the sliding surface morphology is polygonal, correlating with lithological interfaces. The burial depth of the sliding surface ranges from 5 to 38 m in Zone I and from 5 to 23 m in Zone II.

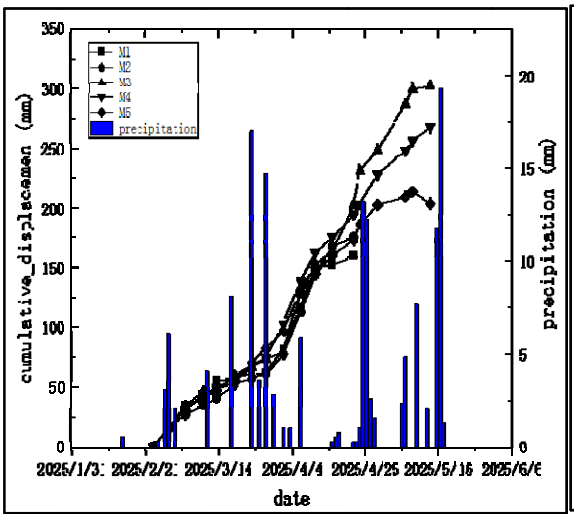


Fig. 3 Rainfall and monitoring point displacement curves.

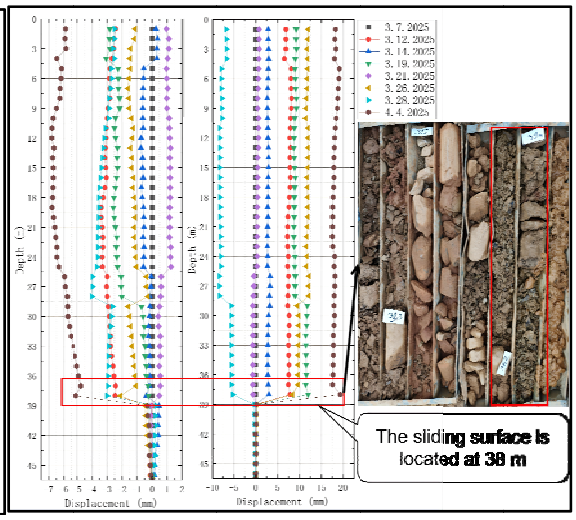


Fig. 4 Deep displacement curve of BH11.

4 Numerical Simulation Analysis

4.1 Model Establishment

This study employed MIDAS, a general-purpose finite element software widely used in geotechnical engineering, for numerical simulation. MIDAS has been extensively applied and validated in geotechnical engineering both domestically and internationally, and the reliability of its computational results provides robust support for the analysis in this study.

For analytical convenience, a typical profile 6-6' (traversing Zone I and Zone II) was selected to establish the numerical model (see Fig. 5). The model dimensions are: horizontal length 300 m, vertical elevation ranging from a minimum of 700 m to a maximum of 780 m. The mesh comprises approximately 21,000 elements.

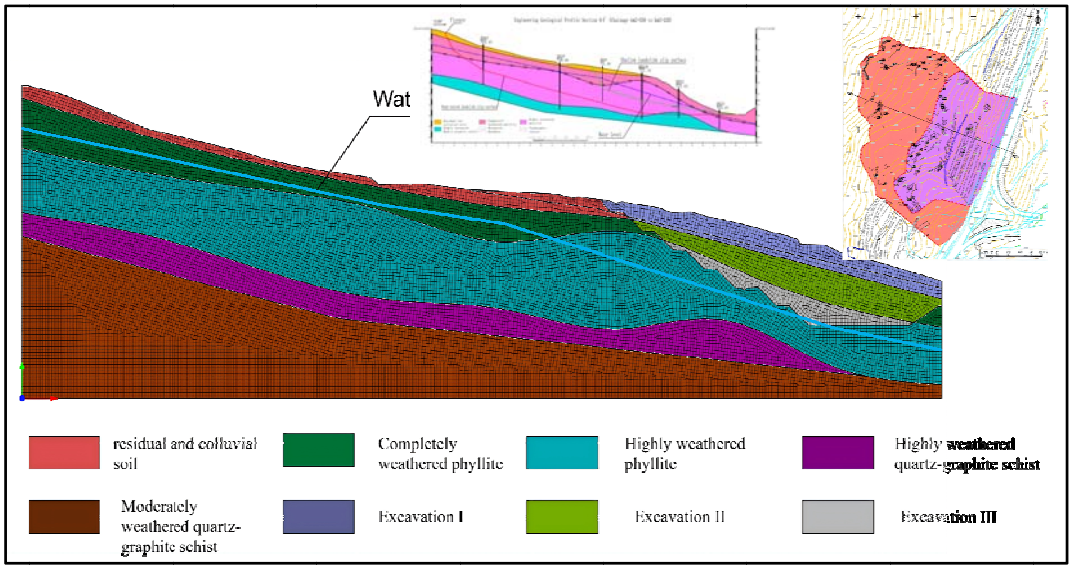


Fig. 5 Numerical model mesh.

Boundary conditions: the bottom is fixed, lateral boundaries are constrained horizontally, and the ground surface is free. Initial condition: self-weight stress field. A linear elastic model was used for static equilibrium calculation of the slope model. The Mohr-Coulomb constitutive model was employed for dynamic calculation. The physical and mechanical parameters of the rock and soil masses were determined comprehensively based on field in-situ tests, laboratory tests, and back analysis, as presented in Table 1.

Table 1. Physical and mechanical parameters of rock and soil mass

Stratum	**Unit weight (kN/m³)**	**Saturated unit weight (kN/m³)**	**Cohesion (kPa)**	**Internal friction angle (°)**	**Elastic modulus (MPa)**	**Poisson's ratio**	**Tensile strength (kPa)**
Residual and deluvial soil	20.9	21.6	17.0	23.0	30	0.30	5
Completely weathered phyllite	22.0	23.6	25.0	19.5	50	0.28	10
Strongly weathered phyllite	25.1	26.4	26.5	19.8	200	0.25	60
Strongly weathered quartz-graphite schist	25.8	26.9	25.0	19.8	300	0.28	65
Moderately weathered quartz-graphite schist	27.0	27.5	150.0	40.0	2000	0.22	800

4.2 Simulation Condition Design

The simulation was conducted in two stages. Stage 1 involved excavation to the current topography. Stage 2 considered the adverse condition of rainfall after excavation, utilizing the back-calculated geotechnical parameters as input to analyze the slope stability via the Strength Reduction Method (SRM).

4.3 Analysis of Simulation Results

Following excavation, the maximum horizontal displacement was concentrated in the mid-lower portion of the slope (Fig. 6a), with a factor of safety calculated as 1.16. Under the superimposed heavy rainfall condition, the displacement at the landslide front further increased, accompanied by expansion of the tensile zone at the trailing edge (Fig. 6b). The factor of safety correspondingly decreased to 1.04.

The equivalent shear strain contour obtained from the SRM analysis reveals a polyline-shaped slip surface extending upward from the shear outlet at the slope toe to the tensile crack zone at the trailing edge (Fig. 6c), closely matching the slip surface identified by monitoring data. Under superimposed rainfall, the zone of high shear strain significantly expanded, indicating complete coalescence of the slip surface (Fig. 6d).

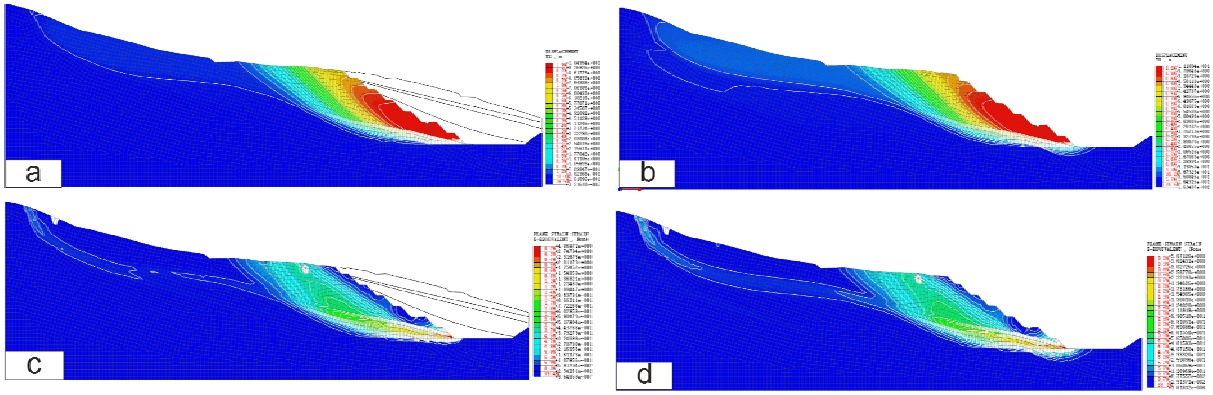


Fig. 6 Comparison of horizontal displacement and equivalent shear strain under different conditions: (a) Displacement after excavation; (b) Displacement under excavation + heavy rainfall; (c) Shear strain after excavation; (d) Shear strain under excavation + heavy rainfall.

5 Analysis and Discussion

5.1 Progressive Coupling Mechanism of Excavation Unloading and Rainfall Infiltration

Excavation unloading is the prerequisite and dominant factor contributing to the instability of this landslide. The formation of a steep free face due to cutting excavation results in the release of horizontal stress within the slope mass, leading to stress field redistribution. Shear stress concentrates at the slope toe, forming a shear yield zone within the strongly weathered phyllite layer. The shear strain contour obtained via SRM (see Fig. 6) indicates that the plastic zone has already expanded intermittently upward from the slope toe at this stage. The embryonic form of the sliding surface is established, and the slope is in a state of critical equilibrium. This stage corresponds to the "constant velocity deformation" segment of the monitoring curve, representing the creep response of the rock mass under constant load.

Rainfall infiltration acts as the triggering factor that transforms the landslide from steady-state creep to accelerated failure. Its mechanism is twofold: first, the attenuation of cohesion and internal friction angle of the sliding zone soil upon saturation (20% strength reduction); second, and more critically, the reduction of effective stress due to increased pore water pressure. For fractured rock masses such as strongly weathered phyllite, rainfall rapidly infiltrates along tension cracks down to the sliding surface, forming transient confined water above the relatively impermeable sliding zone. The resulting buoyancy effect directly counteracts the normal stress on the sliding surface, substantially reducing the shear resistance. Furthermore, the relatively small decrease in the factor of safety accompanied by a sharp increase in deformation rate suggests that under critical conditions, minor external disturbances

can elicit significant deformation responses—a typical characteristic of a slope entering a nonlinear accelerated failure stage.

In summary, the hazard mechanism of this landslide can be summarized as: excavation unloading governs the initiation of the sliding surface and the remodeling of the stress field, while rainfall infiltration triggers the coalescence of the sliding surface and deformation acceleration (see Fig.7). The two processes exhibit a "progressive coupling" relationship. Had there been only excavation without rainfall, the landslide might have remained in a slow creep state for a long time; had there been only rainfall without excavation, the original slope with a gradient of 17°~27° could likely have remained stable.

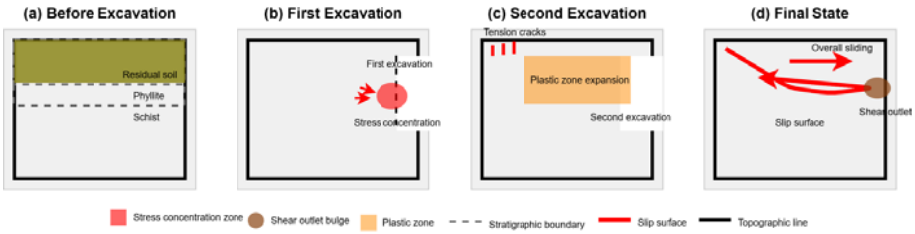


Fig. 7 Schematic diagram of retrogressive landslide instability mechanism.

5.2 Spatiotemporal Differentiation of Retrogressive Landslide Deformation

The deformation monitoring data in this study exhibit significant spatial heterogeneity and temporal phasing, reflecting the unique spatiotemporal evolution pattern characteristic of retrogressive landslides.

Spatially, the surface displacement distribution follows a pattern of "larger in the middle, smaller at the edges." Monitoring point M3, located in the thick central part of the sliding mass, recorded a cumulative displacement of 310.2 mm, whereas point M1 at the rear edge recorded only 175.2 mm. This phenomenon is closely related to the deformation sequence of retrogressive landslides. Following excavation at the toe, the leading edge first undergoes shear creep, creating an unloading zone. Subsequently, the central part of the sliding mass experiences retrogressive tensile deformation due to loss of support from the leading edge, leading to cumulative displacement. The rear edge, under tensile stress, develops arc-shaped tension cracks but undergoes smaller overall displacement. The maximum displacement at M3 is attributed to its position in the transition zone between the traction at the front and the tension at the rear; it is subjected to both the pushing force from the upper sliding mass and the pulling effect from the unloaded front, resulting in a displacement superposition effect. Additionally, drilling revealed that the maximum thickness of the sliding mass in Zone I reaches 38 m, considerably greater than the 23 m in Zone II. The greater gravitational potential energy stored in the thicker sliding mass is another significant geological factor contributing to the displacement disparity.

Temporally, the deformation process can be divided into three stages: constant velocity deformation (Feb 24 – Mar 10), accelerated deformation (Mar 10 – Apr 22), and accelerated creep (Apr 22 – May 14). Notably, the opening and propagation of rear-edge cracks occurred earlier in time than the acceleration of displacement in the central part. Field investigations indicated that rear-edge cracks were already prominently visible in late February (with apertures of 20–38 cm), whereas the acceleration of surface displacement commenced in mid-March following the rainfall. This indicates that retrogressive landslides exhibit a "top-down" sequence of crack propagation but a "bottom-up" sequence of displacement response. The former represents a tensile response to stress release, while the latter is a kinematic response to shear creep along the sliding surface. The spatiotemporal separation of these two phenomena is a significant marker distinguishing retrogressive landslides from thrust-type landslides.

6 Conclusion

This paper takes a retrogressive landslide on a highway in North Macedonia as the research object. Comprehensive methods including surface crack investigation, surface displacement monitoring, deep displacement monitoring, and MIDAS numerical simulation were employed to systematically analyze the deformation characteristics and instability mechanism of the landslide. The main conclusions are as follows:

(1) The landslide is a typical deep-seated retrogressive landslide with a volume of approximately 61×10^4 m³. Arc-shaped tension cracks are well-developed at the rear edge. The sliding surface is located within the completely to strongly weathered phyllite layer, with a maximum burial depth of 38 m. The landslide is currently in an accelerated creep stage.

(2) Surface monitoring reveals a primary sliding direction of 110°~162° and a maximum cumulative displacement of 310.2 mm. Deformation evolves through three stages: constant velocity, acceleration, and accelerated creep. The abrupt increase in displacement rate after mid-March is closely related to rainfall infiltration. Deep monitoring accurately identified the sliding surface depth at 38 m.

(3) MIDAS simulations demonstrate that excavation unloading leads to shear stress concentration at the slope toe, causing the plastic zone to expand upward. Superimposed rainfall softens the sliding zone, leading to full coalescence of the shear strain band and a reduction of the factor of safety from 1.16 to 1.04, confirming the triggering role of rainfall in landslide acceleration.

(4) The failure mechanism of the landslide can be summarized as: "Excavation unloading dominance → Local yielding → Rainfall infiltration softening → Progressive coalescence → Overall sliding." The research findings can provide a reference for the mechanism analysis and mitigation design of deep-seated retrogressive landslides.

References

Yin Y P (2000) Theory and practice of landslide control engineering in China. Hydrogeology & Engineering Geology 27(1): 5-10.

Zheng Y R, Chen Z Y, Wang G X, et al. (2007) Slope and landslide engineering treatment. People's Communications Press, Beijing.

Xu Q, Tang M G, Xu K X, et al. (2008) Study on spatiotemporal evolution laws and early warning prediction of landslides. Chinese Journal of Rock Mechanics and Engineering (06): 1104-1112.

Xu Q, Chen G Q, Wei T, et al. (2025) Study on the dynamic variation characteristics of stress-sliding force-deformation during the formation process of sudden landslides. Chinese Journal of Rock Mechanics and Engineering 44(01): 1-15.

Chen Z Y (2003) Stability analysis of soil slopes: Principles, methods, and programs. China Water & Power Press, Beijing.

Zheng Y R (2012) Development and application of numerical limit analysis methods in geotechnical engineering. Chinese Journal of Rock Mechanics and Engineering 31(07): 1297-1316.

Zhang H X, Zuo S Y, Li H J, et al. (2019) Formation mechanism and treatment effect evaluation of a high-steep retrogressive landslide group. Journal of Guizhou University (Natural Sciences) 36(01): 21-28. DOI:10.15958/j.cnki.gdxbzrb.2019.01.05.

Wang J, Hu X W, He K, et al. (2021) Numerical simulation of deformation and failure mechanism of Boli Village landslide in Yanyuan County based on FLAC-3D. Journal of Geological Hazards and Environment Preservation 32(03): 11-17.